Journal Pre-proofs

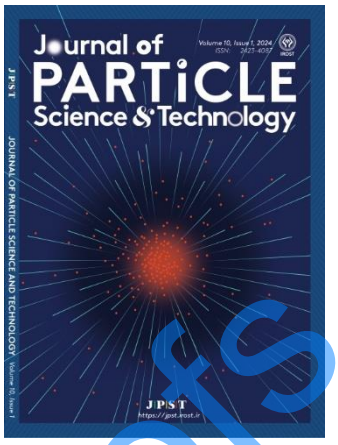

Device-Level Analysis and Optimization of a Novel $YbZrSe_3$-Based Chalcogenide Perovskite Solar Cell: Thickness, Defect, and Band Alignment Optimization

Zihab Sohbatzadeh

DOI: https://doi.org/10.22104/jpst.2026.8508.1301
Manuscript number: JPST-2608-1301

To appear in: *Journal of Particle Science and Technology (JPST)*

Received Date: 22 August 2026
Received Date in revised form: 6 September 2026
Accepted Date: 9 September 2026

Please cite this article as: Sohbatzadeh, Z., Device-Level Analysis and Optimization of a Novel $YbZrSe_3$-Based Chalcogenide Perovskite Solar Cell: Thickness, Defect, and Band Alignment Optimization, *Journal of Particle Science and Technology* (2026), doi: https://doi.org/10.22104/jpst.2026.8508.1301

Device-Level Analysis and Optimization of a Novel $YbZrSe_3$-Based Chalcogenide Perovskite Solar Cell: Thickness, Defect, and Band Alignment Optimization

Zihab Sohbatzadeh

Department of Physics, University of Sistan and Baluchestan, Zahedan, Iran

Abstract

$YbZrSe_3$ is an emerging lead-free chalcogenide absorber with a favorable bandgap for thin-film photovoltaics, but a systematic, device-level optimization of $YbZrSe_3$-based solar cells has not previously been reported. Here, SCAPS-1D simulation is used to address this gap through a sequential optimization strategy, in which each device parameter was tuned in turn while holding the previously optimized parameters fixed. The influence of interface defect density at both the ETL/absorber and absorber/HTL junctions was first examined, revealing that the absorber/HTL interface is markedly more sensitive to defect-induced recombination, with degradation roughly three times larger than at the ETL/absorber interface. Subsequent optimization of absorber thickness (0.7 μm), bulk defect density (10^{14} cm^{-3}), acceptor doping density (10^{17} cm^{-3}), electron affinity (3.7 eV, corresponding to a favorable spike-like band alignment), and electron mobility (100 cm^2/Vs) progressively improved device performance. The fully optimized device achieved a simulated power conversion efficiency of 17.50%, with an open-circuit voltage of 1.1168 V, a short-circuit current density of 18.52 mA/cm^2, and a fill factor of 84.60%, compared with 14.05% for the unoptimized baseline. Recombination current analysis confirmed that interfacial recombination at the absorber/HTL junction dominates the total losses (over 97.5%) even after optimization, while quantum efficiency simulations showed a broad response exceeding 90% between 380 and 550 nm. These results provide the first systematic optimization framework and performance benchmark for $YbZrSe_3$-based solar cells, identifying absorber/HTL passivation as the key route to further gains.

Keywords: SCAPS-1D Simulation, $YbZrSe_3$, Chalcogenide Perovskite Solar Cell, Interface Defect, Device Optimization

1. Introduction

Global demand for clean, sustainable energy has driven rapid growth in photovoltaic technology, with power conversion efficiencies (PCE) of organic–inorganic lead-halide perovskite solar cells now rivaling established crystalline-silicon technology [1]. Despite this progress, commercial deployment remains constrained by the intrinsic toxicity of lead and by limited long-term operational stability under heat, moisture, and illumination [2]. These limitations have motivated a decade-long search for lead-free, environmentally benign absorber materials that retain the favorable optoelectronic character of halide perovskites while avoiding their principal liabilities.

Chalcogenide perovskites (AMX_3, X = S, Se) have emerged as one of the most promising such alternatives, combining high optical absorption coefficients, tunable direct bandgaps, and strong resistance to degradation [2]. This materials class was first proposed on theoretical grounds by Sun et al. [3], who identified several ABX_3 compositions - including $BaZrS_3$ - with bandgaps and absorption properties suited to single-junction photovoltaics. Subsequent experimental work has confirmed many of these predictions: $BaZrS_3$ exhibits an exceptionally strong, near-band-edge absorption coefficient exceeding 10^5 cm^{-1} [4], can be grown as a thin film by sputtering and rapid thermal sulfurization [5], and its bandgap can be tuned toward the Shockley–Queisser optimum through Ti-alloying [6]. To date, most chalcogenide-perovskite research has accordingly focused on alkaline-earth A-site compositions - principally $BaZrS_3$, together with related Ca- and Sr-based analogues - owing to their favorable phase stability and experimentally accessible synthesis routes [2].

Recently, Li et al. [7] extended this design space by proposing Yb^{2+} as an alternative A-site cation, theoretically identifying the new compound family $YbMX_3$ (M = Zr, Hf; X = S, Se) via first-principles calculations. Among these, $YbZrSe_3$ was found to exhibit superior thermodynamic phase stability, good mechanical and dynamical stability, and a direct bandgap in the 1.3–1.7 eV range together with a high visible-light absorption coefficient and low exciton binding energy - properties that led the

authors to predict a theoretical maximum photovoltaic efficiency of approximately 32% at a 1 μm absorber thickness [7]. However, this efficiency estimate, like most first-principles-derived photovoltaic projections, is based on idealized optical absorption and Shockley–Queisser-type arguments; it does not account for defect-mediated recombination, interfacial band alignment, transport-layer selection, or carrier-transport losses that ultimately govern the performance of a real device stack.

Numerical device simulation provides the necessary bridge between such first-principles material predictions and realistic, defect-aware device performance. The Solar Cell Capacitance Simulator (SCAPS-1D), which self-consistently solves the Poisson and carrier-continuity equations across a multilayer device stack, is among the most widely used tools for this purpose and has been extensively validated against experimental current–voltage, capacitance–voltage, and quantum-efficiency data for polycrystalline thin-film solar cells [8,9]. The centrality of defect and interface engineering to this task is well established even for mature halide perovskite devices: detailed device modelling of methylammonium lead iodide solar cells has shown that trap-assisted recombination at interfaces, rather than within grain interiors, is typically the dominant loss channel limiting open-circuit voltage [10]. There is no a priori reason to expect chalcogenide perovskite devices to behave differently, underscoring the need to treat interface defect density as a first-order design variable rather than a secondary refinement.

A growing body of SCAPS-1D studies has applied this approach to chalcogenide-perovskite and related chalcopyrite absorbers. For $BaZrS_3$, reported efficiencies range from under 20% to over 30% depending strongly on the choice of electron- and hole-transport layers, absorber defect density, and interfacial engineering [11–13]. Closer to the present absorber, Se-substituted chalcogenide perovskites have also been explored: a SCAPS-1D study of $BaZrSe_3$ identified absorber thickness and bandgap as dominant performance levers [14], while a broader survey of $ABSe_3$ (A = Ca, Ba; B = Zr, Hf) absorbers projected power conversion efficiencies exceeding 30% once carrier

concentration and transport-layer selection were optimized [15]. For the structurally related chalcopyrite $CuTlS_2$ absorber, a SnS_2/NiO transport-layer combination combined with systematic defect and band-alignment optimization recently yielded a simulated PCE of 32.98% [16]. These studies collectively demonstrate that realizable device efficiency in this materials class is governed as much by interface quality, transport-layer selection, and band alignment as by the intrinsic optoelectronic merit of the absorber itself - underscoring the need for a systematic, device-level optimization study specifically for $YbZrSe_3$.

In this work, we present, to the best of our knowledge, the first device-level SCAPS-1D investigation of a $YbZrSe_3$-based solar cell, adopting an FTO/TiO_2/$YbZrSe_3$/Spiro-OMeTAD/Au architecture consistent with widely used TiO_2/Spiro-OMeTAD transport-layer stacks reported for chalcogenide-perovskite absorbers, including an architecture-matched $BaZrS_3$ study [11,17]. Rather than performing a single global optimization, we adopt a sequential, single-parameter optimization strategy: the ETL/absorber and absorber/HTL interface defect densities, absorber thickness, absorber bulk defect density, acceptor doping density, electron affinity, and electron and hole mobility are each optimized in turn, with every optimum carried forward as the fixed baseline for the subsequent sweep. This approach yields not only a final optimized device but also a quantitative map of critical defect-density and band-alignment thresholds, together with a mechanistic identification - through voltage-dependent recombination-current decomposition, equilibrium band-diagram analysis, and quantum-efficiency spectroscopy - of the dominant loss channel that ultimately limits performance. The remainder of this paper is organized as follows: Section 2 describes the simulation framework, device structure, and material parameters; Section 3 presents the sequential optimization results and device-physics analysis; and Section 4 summarizes the principal conclusions and their implications for future experimental development of $YbZrSe_3$-based photovoltaics.

We note that numerical device simulation of newly proposed absorber materials is a well-established and widely published methodology in the chalcogenide- and halide-perovskite

photovoltaics field: SCAPS-1D studies of emerging absorbers routinely precede experimental fabrication by several years and provide the quantitative performance targets and design guidelines - critical defect-density thresholds, favorable band-alignment windows, and transport-layer selection criteria, among others - that subsequently motivate and guide experimental synthesis efforts [11-17]. Because $YbZrSe_3$ was proposed only very recently on purely theoretical, first-principles grounds [7], with no device-level simulation or experimental realization yet reported, the present work is intended to provide exactly this kind of theoretical-to-device bridge: a first, systematic, device-level performance benchmark and set of design guidelines to inform future experimental development of this absorber, rather than a claim of experimental validation.

2. Simulation Framework and Methodology

2.1. Device structure and simulation tool

The device architecture investigated in this work, shown schematically in Figure 1, is FTO/TiO_2 (ETL)/$YbZrSe_3$ (absorber)/Spiro-OMeTAD (HTL)/Au (back contact), an FTO/TiO_2/Spiro-OMeTAD transport-layer stack matching the architecture adopted in a prior $BaZrS_3$ SCAPS-1D study [17]. Fluorine-doped tin oxide (FTO) serves as the transparent front electrode: owing to its high visible-range transmittance, low sheet resistance, and superior chemical and thermal stability relative to competing transparent conducting oxides, FTO remains the most widely adopted front-contact material for chalcogenide- and halide-perovskite thin-film photovoltaics [27]. TiO_2 was selected as the electron-transport layer (ETL) for its well-documented capacity to selectively extract and transport photogenerated electrons while blocking holes, its favorable conduction-band alignment with a broad range of narrow-bandgap absorbers, and its extensive precedent in both experimental and SCAPS-1D-simulated perovskite and chalcogenide-perovskite devices [25]. The $YbZrSe_3$ layer absorbs incident light and generates electron–hole pairs. Spiro-OMeTAD was selected as the hole-transport layer (HTL) for its favorable valence-band alignment, well-characterized hole-mobility and

doping behavior, and its status as the most extensively benchmarked organic HTL in the perovskite-photovoltaics literature [26]; Au was retained as the back contact for its high work function and its consequent near-ohmic behavior at the interface with wide-gap p-type absorbers. We note, however, that inorganic hole-transport materials such as Cu_2O and NiO are promising alternatives on stability grounds, since Spiro-OMeTAD is known to be hygroscopic and thermally less stable than inorganic hole conductors; a systematic comparison of such transport-layer choices is identified as a valuable direction for future work building on the present absorber-level optimization.

All simulations were performed using SCAPS-1D, a widely validated one-dimensional device simulator originally developed at Ghent University for the $CuInSe_2$ and CdTe thin-film solar-cell families [18,19] and subsequently extended to accommodate multivalent defect charge states [20] and intra-band tunneling at heterojunction interfaces [21]. The simulator self-consistently solves the Poisson equation together with the electron and hole continuity and current-density equations under the Gummel iterative decoupling scheme [22], in which the electrostatic potential and the electron and hole quasi-Fermi levels are updated sequentially at every bias point until convergence is reached:

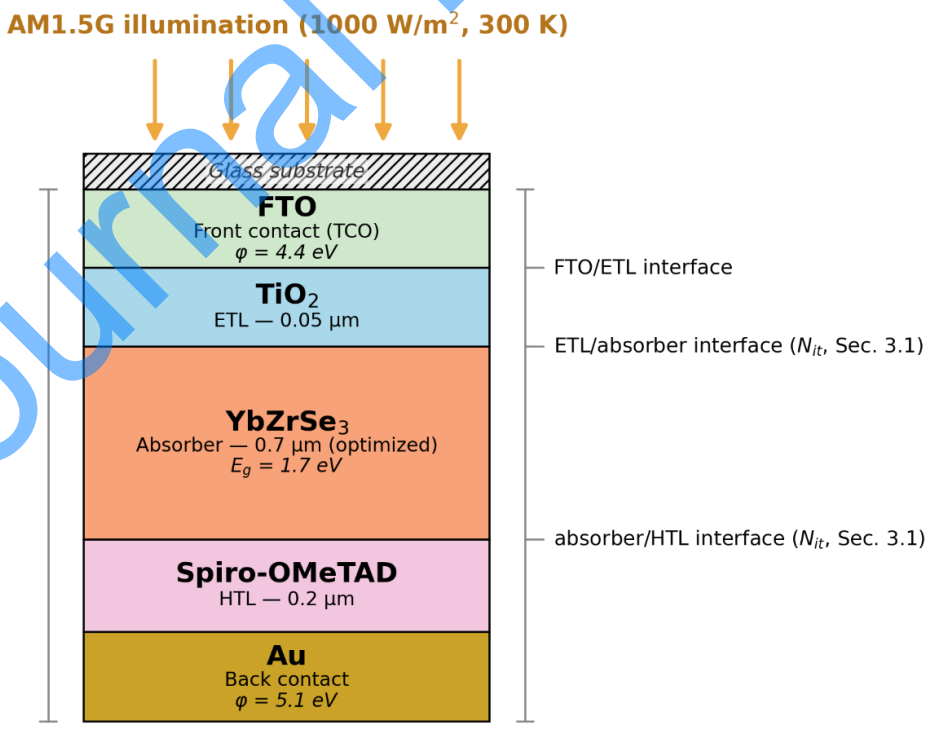

Fig. 1. Schematic cross-section of the simulated device.

To describe the electrostatic behavior and charge-carrier transport in the simulated devices, the SCAPS-1D solver simultaneously solves the coupled Poisson equation and electron and hole continuity equations. The governing equations used in the numerical simulations are given in Eqs. (1)–(5).

$$\partial/\partial x(\, \varepsilon_0 \varepsilon \, \partial\Psi/\partial x \,) = -q(\, p - n + N_D^{+} - N_A^{-} + \rho_{def}/q \,) \quad (1)$$

$$-\partial J_n/\partial x - U_n + G = \partial n/\partial t \quad (2)$$

$$-\partial J_p/\partial x - U_p + G = \partial p/\partial t \quad (3)$$

$$J_n = -\mu_n \, n \, (q) \, \partial E_{Fn}/\partial x \quad (4)$$

$$J_p = +\mu_p \, p \, (q) \, \partial E_{Fp}/\partial x \quad (5)$$

Here, ε_0 is the vacuum permittivity; ε is the relative dielectric permittivity; Ψ is the electrostatic potential; q is the elementary charge; p and n are the free-hole and free-electron concentrations, respectively; N_D^{+} and N_A^{-} are the ionized donor and acceptor densities, respectively; ρ_{def} is the charge density trapped at defects; J_n is the electron current density; U_n is the net Shockley–Read–Hall recombination rate for electrons; G is the optical generation rate; t is time; J_p is the hole current density; U_p is the net Shockley–Read–Hall recombination rate for holes; μ_n is the electron mobility; E_{Fn} is the electron quasi-Fermi level; μ_p is the hole mobility; and E_{Fp} is the hole quasi-Fermi level. The optical generation profile G(x) at each depth x was computed by SCAPS-1D from the Beer–Lambert absorption of the AM1.5G reference spectrum [29], using the wavelength-dependent absorption coefficient assigned to every layer in the stack; for the $YbZrSe_3$ absorber, the absorption coefficient and complex refractive index were taken from the first-principles optical calculations reported for this materials family [7]. Absorption profiles were included for the FTO front contact and the TiO_2 and Spiro-OMeTAD transport layers, and not only for the absorber, so that the simulated

short-circuit current and external quantum efficiency (Section 3.9) account for parasitic, non-absorber optical losses rather than treating the transport layers as optically inert.

2.2. Material parameters and optimization strategy

Rather than a single global optimization, a sequential, single-parameter strategy was adopted: seven device parameters - the ETL/absorber interface defect density (N_{it}), the absorber/HTL interface defect density (N_{it}), absorber thickness, absorber bulk defect density (N_t), absorber acceptor doping density (N_A), absorber electron affinity (χ), and absorber electron and hole mobility (μn, μp) - were each varied in turn over a physically motivated range while all previously optimized parameters were held fixed at their optimum value. This approach, detailed sequentially in Sections 3.1–3.6, yields both a final optimized device configuration and an explicit map of the critical defect-density and band-alignment thresholds that bound acceptable device performance. Where a parameter's response was monotonic without saturation (Sections 3.2, 3.4, 3.7), the optimum was defined using a 5% maximum-tolerable relative PCE loss criterion relative to the defect-free or asymptotic limit; where a genuine interior maximum in PCE was observed (Sections 3.4 and 3.5), the optimum was taken directly as the sweep value that maximized PCE.

This sequential, single-parameter methodology was favored over a simultaneous multi-parameter or statistically sampled (e.g., Latin-hypercube or machine-learning-assisted) joint optimization because it provides direct, physically interpretable visibility into the sensitivity of each individual loss mechanism, an approach with established precedent in SCAPS-1D studies of both chalcogenide-perovskite [12] and structurally related chalcopyrite absorbers. Its principal limitation, common to all one-parameter-at-a-time sweep methodologies, is that it explores only a one-dimensional slice of the multi-dimensional parameter space at each step and therefore risks converging to a local rather than a global optimum; a fully coupled statistical or machine-learning-assisted joint optimization is identified as a natural direction for future work on this materials system.

Table 1 summarizes the material parameters used for the ETL, absorber, and HTL layers, as implemented in the SCAPS-1D Layer Properties panel for this device, together with the sequentially optimized absorber parameters established in Sections 3.1–3.6 of this work.

Table 1. Material parameters used in the SCAPS-1D simulations.

Parameter	**TiO_2 (ETL)**	**$YbZrSe_3$ (Absorber)**	**Spiro-OMeTAD (HTL)**
Thickness (μm)	0.05	0.7 (optimized, Sec. 3.2)	0.2
Bandgap (eV)	3.2	1.7	3.0
Electron affinity (eV)	4.0	3.7 (optimized, Sec. 3.5)	2.2
Dielectric permittivity (relative)	9	8.972	3
CB effective density of states (cm^{-3})	2.2×10^{18}	1×10^{19}	1×10^{19}
VB effective density of states (cm^{-3})	1.8×10^{19}	1×10^{19}	1×10^{19}
Electron thermal velocity (cm/s)	1×10^{7}	1×10^{7}	1×10^{7}
Hole thermal velocity (cm/s)	1×10^{7}	1×10^{7}	1×10^{7}
Electron mobility (cm^2/Vs)	20	100 (optimized, Sec. 3.6)	1×10^{-4}
Hole mobility (cm^2/Vs)	0.1	10 (Sec. 3.6)	1×10^{-2}
Donor density N_D (cm^{-3})	1×10^{18}	0	0
Acceptor density N_A (cm^{-3})	1×10^{15}	1×10^{17} (optimized, Sec. 3.4)	1×10^{18}
Bulk defect density N_t (cm^{-3})	None added (ideal ETL)	1×10^{14} (optimized, Sec. 3.3)	None added (ideal HTL)
N_{it} - ETL/absorber interface (cm^{-2})	-	1×10^{10} (optimized, Sec. 3.1)	-
N_{it} - absorber/HTL interface (cm^{-2})	-	1×10^{11} (Sec. 3.1)	-

Because $YbZrSe_3$ was proposed only very recently on purely theoretical grounds [7], it is useful to distinguish, among the parameters in Table 1, which are grounded in first-principles calculations and which are modeling assumptions. The bandgap (1.7 eV) is taken directly from the first-principles calculations of Li et al. [7], who report a direct bandgap in the 1.3–1.7 eV range for $YbZrSe_3$ depending on the specific computational method and structural assumptions used; the upper bound

of this range was selected here both because it lies closer to the Shockley–Queisser optimum for single-junction absorbers and because Li et al. [7] associate their highest predicted theoretical efficiency (≈ 32% at 1 μm thickness) with a bandgap near this value — this choice therefore represents a reasonable, literature-consistent starting point rather than an unambiguously established single value, since no experimental bandgap measurement yet exists for this material. The electron affinity, dielectric permittivity, effective densities of states, and doping/defect densities have likewise not yet been measured experimentally for this compound and are assumed values, chosen either by analogy with structurally related, better-characterized chalcogenide perovskites ($BaZrS_3$, $BaZrSe_3$ [11,14]) or as physically reasonable estimates that keep the device in the non-degenerate regime. The electron mobility of 100 $cm^2/V{\cdot}s$ adopted following Section 3.6 is similarly not an experimentally measured value; it was selected as the upper end of the range explored in the mobility sweep, within which PCE was still increasing without a clear plateau, and should be regarded as an upper-bound design target for future thin-film growth rather than a demonstrated material property. The interface defect densities adopted as safety-margin baselines in Section 3.1.4 ($N_{it} = 10^{10}$ cm^{-2} at the ETL/absorber interface and 10^{11} cm^{-2} at the absorber/HTL interface) fall within the range commonly measured or assumed for well-passivated oxide/absorber and absorber/organic-HTL interfaces in the halide- and chalcogenide-perovskite literature, but have not been demonstrated experimentally for $YbZrSe_3$-based junctions specifically, and would likely require interfacial passivation strategies analogous to those developed for halide perovskite devices. Accordingly, the terms “optimum” and “optimized value” used throughout Section 3 refer to the optimum identified within the specific one-parameter-at-a-time range investigated in this sequential study and should not be read as a claim of a global or experimentally validated optimum; and, since no experimental $YbZrSe_3$ device has yet been fabricated, all reported performance figures throughout this manuscript represent SCAPS-1D predictions rather than measured device characteristics.

The front (FTO) and back (Au) contacts were assigned typical work functions of 4.4 eV and 5.1

eV, respectively, with surface recombination velocities of 10^7 cm/s (majority carrier) and 10^5 cm/s (minority carrier); these contact assumptions follow standard SCAPS-1D defaults widely used in comparable chalcogenide-perovskite and chalcopyrite device studies [11,14,17] and are consistent with the physical and electrical characteristics of FTO thin films summarized in a recent review of transparent conducting oxides for thin-film photovoltaics [27], and should be replaced with the exact values used in this study's Action Panel settings if these differ.

2.3. Interfacial band alignment

The conduction- and valence-band offsets at each heterojunction (FTO/TiO_2, TiO_2/$YbZrSe_3$, and $YbZrSe_3$/Spiro-OMeTAD) are determined within SCAPS-1D by the electron-affinity (Anderson) model [28], in which the conduction-band offset ΔE_c equals the difference in electron affinity χ between the two adjacent layers, and the valence-band offset ΔE_v follows from the additional difference in bandgap E_g:

$$\Delta E_c = \chi_1 - \chi_2 \quad (6)$$

$$\Delta E_v = (\chi_2 + E_{g2}) - (\chi_1 + E_{g1}) \quad (7)$$

For the optimized device parameters listed in Table 1 (χ_{TiO2} = 4.0 eV, $\chi_{YbZrSe3}$ = 3.7 eV with E_g = 1.7 eV, and χ_{Spiro} = 2.2 eV with E_g = 3.0 eV), this model yields a small conduction-band spike of $\Delta E_c \approx 0.3$ eV at the ETL/absorber junction - consistent with the spike-type alignment identified in Section 3.5 as favorable for suppressing interface recombination while remaining low enough not to impede electron extraction - and a large conduction-band offset of $\Delta Ec = \chi_{YbZrSe3} - \chi_{Spiro} = 3.7 - 2.2 \approx 1.5$ eV at the absorber/HTL junction that effectively blocks electron back-flow toward the back contact. This offset-driven picture is consistent with the pronounced sensitivity of device performance to the ETL/absorber and absorber/HTL interface defect densities established in Section 3.1, since band-

offset-dependent tunneling and thermionic-emission recombination pathways at a heterojunction are strongly modulated by the occupation of interface trap states [20,21].

2.4. Defect and recombination modeling assumptions

Bulk defects in the $YbZrSe_3$ absorber and interface defects at the ETL/absorber and absorber/HTL junctions were modeled as single-level Shockley–Read–Hall trap states [23,24], following the standard SCAPS-1D defect formalism [8,9] and its extension to multivalent charge-state defects [20] (not required for the neutral, single-level treatment adopted here). Unless otherwise noted in Sections 3.2–3.4, defect energy levels were placed at midgap ($E_t = E_i$) with a uniform spatial distribution through the layer thickness, and electron and hole capture cross-sections were fixed at 1×10^{-15} cm^2, consistent with values commonly adopted for chalcogenide-perovskite and chalcopyrite absorbers in the absence of directly measured capture-cross-section data for this materials family [12,14]. Because no experimentally measured capture cross sections or thermal velocities are yet available for $YbZrSe_3$ - an absorber proposed only very recently on purely theoretical grounds [7] - these values were instead adopted from prior SCAPS-1D studies of structurally related chalcogenide-perovskite and chalcopyrite absorbers [12,14], and are additionally consistent with generic values tabulated for compound semiconductors of comparable bandgap [30]; this substitution is noted here as a modeling assumption necessitated by the current absence of material-specific measurements. Electron and hole thermal velocities were fixed at 1×10^7 cm/s for all layers (Table 1), following standard SCAPS-1D defaults consistent with typical values tabulated for compound semiconductors [30].

Band-to-band radiative and Auger recombination coefficients were retained at SCAPS-1D default values for this materials class, since no experimentally measured coefficients are yet available for $YbZrSe_3$; Shockley–Read–Hall recombination is expected to dominate the total recombination current in the defect-density regime explored in Sections 3.2–3.4, consistent with the voltage-dependent recombination-current decomposition presented in Section 3.8. All layers were treated as

compositionally uniform (non-graded), with abrupt heterojunctions at every interface; SCAPS-1D's capability to simulate spatially graded band gaps and compositions [31] was not exercised in this study, since no experimental compositional-grading profile has yet been reported for $YbZrSe_3$-based devices.

3. Results and discussion

3.1. Impact of Interface Defect Density on Photovoltaic Performance

3.1.1. ETL/Absorber Interface

To evaluate the stability and reliability of the device, the influence of interface defect density (N_{it}) at the ETL/absorber interface was investigated. The variations of key photovoltaic parameters, including power conversion efficiency (PCE), fill factor (FF), short-circuit current density (Jsc), and open-circuit voltage (Voc), are presented in Figure 2.

As shown in Figure 2, all four parameters exhibit a clear dependence on the defect density. When N_{it} increases from 10^{10} to 10^{13} cm^{-2}, a significant degradation in performance is observed: Voc drops from 0.9265 V to 0.8907 V (Figure 2, bottom panel), and Jsc shows a slight but noticeable decline from 19.413 to 19.349 mA/cm^2 (Figure 2, third panel). This behavior is attributed to increased recombination rates at the interface, which suppress charge carrier extraction.

FF and PCE are particularly sensitive to these defects, decreasing from 85.58% to 82.49% and from 15.39% to 14.22%, respectively, over the same range, as seen in the top two panels of Figure 2. Beyond $N_{it} = 10^{14}$ cm^{-2}, all four curves in Figure 2 flatten and stabilize (Voc ≈ 0.888 V, FF ≈ 82.11%, PCE ≈ 14.05%), suggesting that the recombination process becomes limited by the saturation of interface states rather than by the trap density itself. These results indicate that maintaining N_{it} below 10^{13} cm^{-2} at the ETL/absorber interface is critical for high-performance, stable device operation.

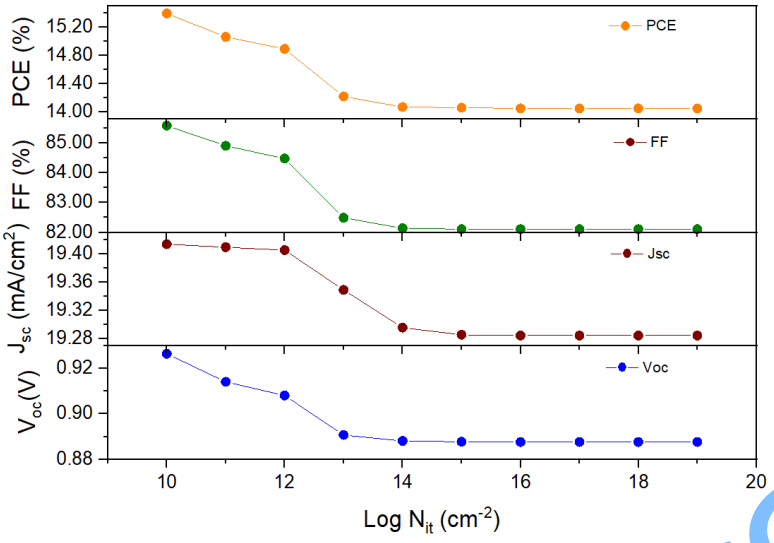

Fig. 2. Simulated photovoltaic parameters versus ETL/absorber interface defect density.

3.1.2. Absorber/HTL Interface

The same procedure was applied to the absorber/HTL (Spiro-OMeTAD) interface, sweeping N_{it} from 10^{10} to 10^{19} cm^{-2} while keeping all other device parameters, including the ETL/absorber interface properties, fixed at their baseline values. The resulting photovoltaic parameters are shown in Figure 3.

As with the ETL/absorber interface, Figure 3 shows all four parameters degrading sharply between $N_{it} = 10^{10}$ and 10^{13}–10^{14} cm^{-2}. In this range, Voc decreases from 1.0109 V to 0.8878 V and FF from 86.97% to 82.12% (Figure 3, bottom and second panels), while PCE drops from 17.07% to 14.07% (Figure 3, top panel); Jsc declines only slightly, from 19.418 to 19.296 mA/cm^2 (Figure 3, third panel). This trend confirms that Shockley–Read–Hall recombination at the absorber/HTL interface becomes the dominant loss channel at elevated defect densities, suppressing hole extraction toward the HTL and thereby reducing Voc and FF.

Beyond $N_{it} \approx 10^{14}$–10^{15} cm^{-2}, all four curves in Figure 3 become essentially flat up to 10^{19} cm^{-2} (Voc ≈ 0.8875 V, FF ≈ 82.10%, PCE ≈ 14.05%), indicating that the interface recombination rate becomes limited by minority-carrier transport to the interface rather than by the trap density itself once this threshold is exceeded.

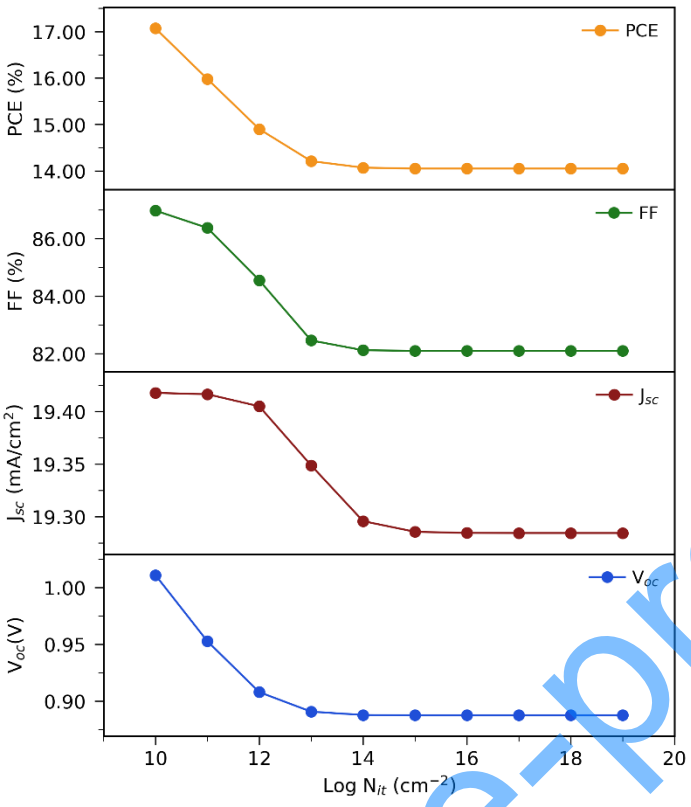

Fig. 3. Simulated photovoltaic parameters versus absorber/HTL interface defect density.

3.1.3. Comparative Sensitivity of the Two Interfaces

Comparing the initial and saturated branches of Figs. 2 and 3, the degradation induced by interface defects is markedly stronger at the absorber/HTL interface than at the ETL/absorber interface: ΔVoc and ΔPCE are roughly three times larger for the absorber/HTL interface. This indicates that hole extraction at the absorber/HTL junction is intrinsically more vulnerable to defect-induced recombination in this device architecture than electron extraction at the ETL/absorber junction. Notably, both curves in Figs. 2 and 3 converge to nearly identical saturated values (Voc ≈ 0.888 V, FF ≈ 82.1%, PCE ≈ 14.05%) at high N_{it}, indicating that once either interface becomes strongly defective, device performance is limited by a common recombination floor set by the remaining junction and the bulk absorber properties. These results suggest that interfacial passivation strategies should be prioritized at the absorber/HTL interface to maximize device stability and efficiency.

Table 2. Photovoltaic response to interface defect density.

Interface	Voc at $N_{it} = 10^{10}$ (V)	Voc saturated (V)	ΔVoc (V)	PCE at $N_{it} = 10^{10}$ (%)	PCE saturated (%)	ΔPCE (pp)
ETL/absorber	0.9265	0.8876	0.039	15.39	14.05	1.34
Absorber/HTL	1.0109	0.8875	0.123	17.07	14.05	3.02

3.1.4. Recommended Interface Defect Density for Optimal Device Performance

Since PCE, FF, and Voc decrease monotonically with increasing N_{it} at both interfaces (no intermediate optimum exists), the practically meaningful design target is not a single "best" N_{it} value but the maximum defect density that can be tolerated before performance departs appreciably from its defect-free limit. This threshold was defined here as the N_{it} at which PCE falls to 95% of its value at $N_{it} = 10^{10}$ cm^{-2} (i.e., a maximum tolerable relative PCE loss of 5%), obtained by linear interpolation of the PCE data in Figs. 2 and 3 on a log(N_{it}) scale.

The resulting thresholds, summarized in Table 3, differ by roughly two orders of magnitude between the two interfaces. For the ETL/absorber interface, N_{it} must remain below approximately 2.5 × 10^{12} cm^{-2} (log N_{it} ≈ 12.4) to stay within the 5% PCE tolerance. For the absorber/HTL interface, the corresponding limit is far stricter, approximately 6.1 × 10^{10} cm^{-2} (log N_{it} ≈ 10.8). This quantitatively confirms that the absorber/HTL interface is the more critical junction to passivate: even a modest increase in N_{it} at this interface (less than one order of magnitude above 10^{10} cm^{-2}) is sufficient to erode the 5% performance margin, whereas the ETL/absorber interface can tolerate roughly two additional orders of magnitude of defect density before the same margin is lost.

Table 3. Interface defect density thresholds for 5% PCE loss.

Interface	PCE at $N_{it} = 10^{10}$ cm^{-2} (%)	Critical N_{it} (cm^{-2}) for ≤ 5% PCE loss	log(Critical N_{it})
ETL/absorber	15.39	~2.5 × 10^{12}	~12.4
Absorber/HTL	17.07	~6.1 × 10^{10}	~10.8

These thresholds should be interpreted as design guidelines rather than fixed physical limits, since the 5% tolerance is a chosen engineering criterion; adopting a stricter or looser tolerance would shift both values consistently. Nonetheless, the roughly two-order-of-magnitude gap between the two interfaces is a robust conclusion, and it is not sensitive to the specific tolerance chosen. Overall, these results indicate that experimental efforts to reduce interfacial trap density in this device architecture, whether through surface treatment, buffer layers, or improved absorber/HTL contact quality, should be prioritized at the absorber/HTL interface, as it offers the greatest potential gain in device stability and efficiency for a given reduction in defect density.

Guided by these thresholds, the interface defect densities used as fixed baseline values in all subsequent simulations (thickness and absorber bulk defect density optimization) were set to N_{it} = 10^{10} cm^{-2} at the ETL/absorber interface and N_{it} = 10^{11} cm^{-2} at the absorber/HTL interface. The ETL/absorber value lies two orders of magnitude below its critical threshold (~2.5 × 10^{12} cm^{-2}), providing a substantial safety margin. For the absorber/HTL interface, however, the adopted baseline (10^{11} cm^{-2}) exceeds its critical threshold (~6.1 × 10^{10} cm^{-2}); based on the sweep data in Figure 3, this corresponds to a PCE of 15.98% versus the defect-free-limit value of 17.07% (at N_{it} = 10^{10} cm^{-2}), i.e., a ~6.4% relative loss, slightly beyond the 5% tolerance margin defined in this section. This should be noted when interpreting the absolute PCE values reported in the following sections; the relative trends and comparisons among the subsequently varied parameters remain valid, since the absorber/HTL interface condition was held fixed throughout.

3.2. Impact of Absorber Layer Thickness on Photovoltaic Performance

To identify the optimal absorber thickness, the $YbZrSe_3$ layer thickness was varied from 0.1 to 1.2 µm in steps of 0.1 µm, and the resulting photovoltaic parameters are shown in Figure 4.

As shown in Figure 4, Jsc rises sharply with thickness at first, from 9.00 to 19.38 mA/cm^2 between 0.1 and 0.5 µm (Figure 4, third panel), then continues to increase more gradually up to 21.68 mA/cm^2

at 1.2 μm, consistent with progressively more complete absorption of incident photons as the optical path length increases. Voc increases modestly and monotonically over the same range, from 0.976 V to 1.031 V (Fig. 4, bottom panel), reflecting the increase in photogenerated carrier density (and hence quasi-Fermi level splitting) with thickness. FF behaves non-monotonically (Figure 4, second panel): it first rises slightly from 86.11% at 0.1 μm to a maximum of 86.60% at 0.3 μm, then decreases steadily to 84.72% at 1.2 μm as the longer transport path and larger absorber volume increase the probability of bulk recombination before carriers reach the contacts.

The combined effect on PCE, shown in the top panel of Figure 4, is a steep initial rise (7.56% to 16.88% between 0.1 and 0.5 μm) that gradually flattens at larger thicknesses, reaching 18.93% at 1.2 μm with clearly diminishing returns beyond approximately 0.7–0.8 μm. Applying the same 5% relative-loss criterion used for the interface defect density analysis (Section 3.1.4), 95% of the maximum PCE (18.93%) corresponds to 17.98%, reached at approximately 0.7 μm (PCE = 17.96% at this thickness). Beyond ~0.7 μm, PCE approaches saturation while FF continues to decline and Jsc gains become marginal (only a further ~5% increase in Jsc between 0.7 and 1.2 μm). Accordingly, an absorber thickness of 0.7 μm was selected as the optimal value and adopted as the fixed baseline thickness in all subsequent simulations, balancing near-maximal photovoltaic performance against unnecessary material usage and bulk-recombination-induced FF loss.

3.3. Impact of Absorber Bulk Defect Density on Photovoltaic Performance

With the absorber thickness fixed at its optimal value (0.7 μm, Section 3.2) and the interface defect densities fixed at their baseline values (Section 3.1.4), the total bulk defect density (Nt) of the $YbZrSe_3$ absorber layer was varied from 10^{10} to 10^{18} cm^{-3} in 9 logarithmically spaced steps, and the resulting photovoltaic parameters are shown in Figure 5.

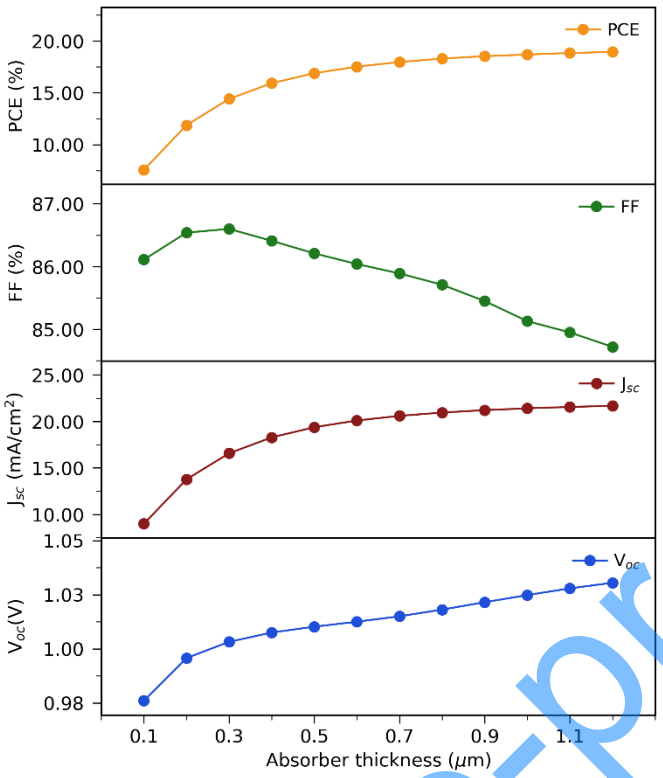

Fig. 4. Simulated photovoltaic parameters versus absorber layer thickness.

As shown in Figure 5, the device response to bulk defect density is qualitatively different from its response to interface defect density: rather than a gradual decline followed by saturation, all four parameters remain essentially unchanged up to N_t = 10^{14} cm^{-3} (PCE = 17.12% at 10^{10} cm^{-3} versus 17.02% at 10^{14} cm^{-3}), then undergo a sharp, threshold-like collapse (Figure 5, all panels). Between 10^{14} and 10^{18} cm^{-3}, FF falls from 85.33% to 22.84% (Figure 5, second panel) and Voc from 0.9656 V to 0.7417 V (Figure 5, bottom panel), while Jsc, initially unaffected, drops precipitously beyond 10^{16} cm^{-3} (20.65 to 3.82 mA/cm^2) as the bulk carrier diffusion length falls below the absorber thickness (Figure 5, third panel). The combined effect on PCE, shown in the top panel of Figure 5, is a collapse from 17.12% to 0.65% between 10^{10} and 10^{18} cm^{-3}, with essentially all of the loss occurring above 10^{14} cm^{-3}. This behavior is consistent with Shockley–Read–Hall recombination becoming bulk-transport-limited once the minority-carrier diffusion length, which scales inversely with the square root of N_t, drops to the order of the absorber thickness, sharply increasing the fraction of photogenerated carriers that recombine before reaching the contacts.

Applying the same 5% relative-loss criterion used in Sections 3.1.4 and 3.2, 95% of the defect-free-limit PCE (17.12% at Nt = 10^{10} cm^{-3}) corresponds to 16.26%, reached by linear interpolation between 10^{14} cm^{-3} (PCE = 17.02%) and 10^{15} cm^{-3} (PCE = 16.20%), giving a critical bulk defect density of approximately 8×10^{14} cm^{-3} (log Nt ≈ 14.9). This threshold is markedly sharper than those found for the interface defects (Section 3.1.4): below it, performance is essentially insensitive to Nt, whereas beyond it, degradation is rapid and catastrophic rather than gradual. Accordingly, a bulk defect density of 10^{14} cm^{-3}, one order of magnitude below this critical threshold, was adopted as the fixed baseline value for the absorber layer in subsequent simulations, consistent with the safety-margin approach used for the ETL/absorber interface in Section 3.1.4.

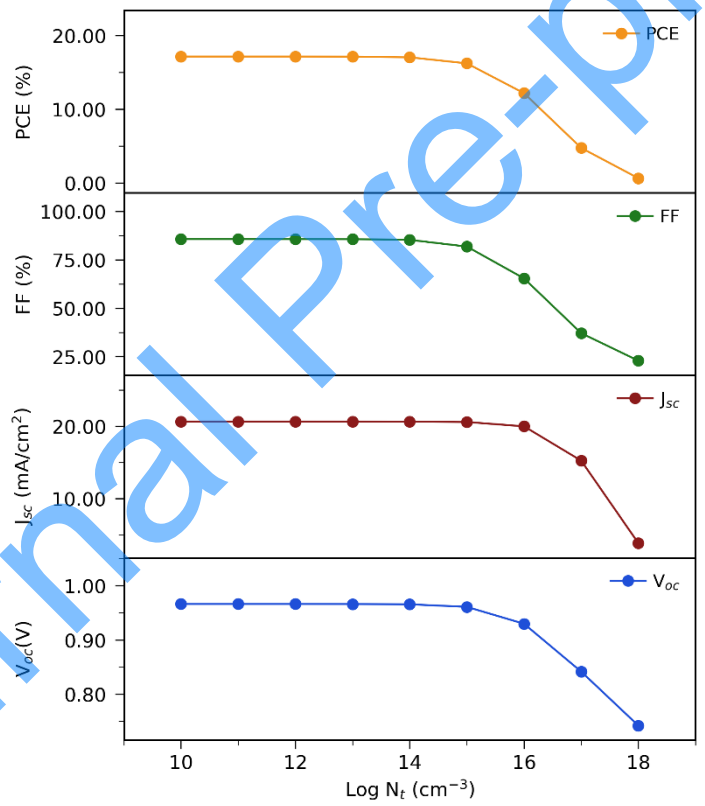

Fig. 5. Simulated photovoltaic parameters versus absorber bulk defect density.

3.4. Impact of Absorber Acceptor Doping Density on Photovoltaic Performance

With the absorber thickness, interface defect densities, and bulk defect density fixed at their previously determined baseline values (Sections 3.1–3.3), the shallow uniform acceptor doping

density (NA) of the YbZrSe3 absorber was varied from 10^{14} to 10^{18} cm^{-3} in logarithmic steps, and the resulting photovoltaic parameters are shown in Figure 6. The sweep was limited to 10^{18} cm^{-3}; beyond this value the doping approaches the degenerate regime (typically above 10^{19}–10^{20} cm^{-3} for this class of semiconductors), where the Boltzmann-statistics and bandgap-narrowing assumptions underlying the standard drift-diffusion model are no longer valid; simulations attempted beyond this range failed to converge to a physically meaningful operating point, consistent with this interpretation.

As shown in Figure 6, Voc increases monotonically and substantially with N_A, from 0.953 V at 10^{14} cm^{-3} to 1.238 V at 10^{17} cm^{-3} (Figure 6, bottom panel), consistent with the higher built-in potential produced by heavier acceptor doping. Jsc decreases monotonically over the same range, from 20.65 to 15.98 mA/cm^2 (Figure 6, third panel), reflecting the progressive narrowing of the quasi-neutral region and increased recombination associated with higher doping. FF behaves non-monotonically (Figure 6, second panel): it declines from 85.97% at 10^{14} cm^{-3} to a minimum of 79.86% at 10^{16} cm^{-3}, then recovers to 83.58% at 10^{18} cm^{-3}, indicating competing effects of an improving built-in field and increasing recombination losses on carrier collection.

Unlike the interface defect density, absorber thickness, and bulk defect density sweeps (Sections 3.1–3.3), each of which varied monotonically toward a saturating or collapsing limit, the doping sweep produces a genuine interior optimum in PCE, shown in the top panel of Figure 6: PCE rises from 16.92% at 10^{14} cm^{-3} to a maximum of 17.89% at 10^{17} cm^{-3}, then falls to 16.32% at 10^{18} cm^{-3}. This peak reflects the trade-off between the Voc gain and the Jsc loss with increasing doping: up to 10^{17} cm^{-3}, the Voc improvement dominates, while beyond this value the loss in Jsc (and the associated FF penalty) outweighs further Voc gains. Accordingly, an acceptor doping density of NA = 10^{17} cm^{-3} was identified as the optimal value and adopted as the fixed baseline doping density for the absorber layer in subsequent simulations.

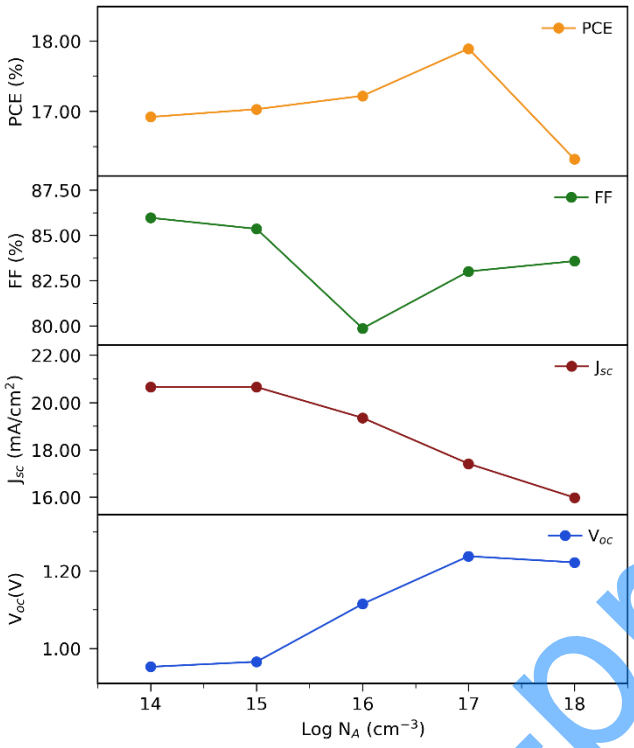

Fig. 6. Simulated photovoltaic parameters versus absorber acceptor doping density.

3.5. Impact of Absorber Electron Affinity on Photovoltaic Performance

With the absorber thickness, interface and bulk defect densities, and acceptor doping density fixed at their previously determined optimal values (Sections 3.1–3.4), the electron affinity (χ) of the YbZrSe3 absorber was varied from 3.4 to 4.3 eV in steps of 0.1 eV about the baseline value (3.8 eV), and the resulting photovoltaic parameters are shown in Figure 7. Since electron affinity directly governs the conduction-band offset at the ETL/absorber interface, this sweep spans both the spike-like alignment regime (lower χ) and the cliff-like alignment regime (higher χ).

As shown in Figure 7, Jsc remains essentially unaffected by χ (20.654–20.666 mA/cm^2, a variation of under 0.1%; Figure 7, third panel), since electron affinity alters band alignment rather than optical absorption. In contrast, Voc, FF, and PCE all respond strongly and non-monotonically (Figure 7, top three panels): each rises from χ = 3.4 eV to a maximum at χ = 3.6 eV (Voc = 1.1322 V, FF = 85.19%, PCE = 19.92%), then declines steadily and steeply through the remainder of the range, reaching Voc = 0.5638 V, FF = 79.07%, and PCE = 9.21% at χ = 4.3 eV.

This behavior is consistent with the well-known spike/cliff transition at the ETL/absorber junction. At $\chi = 3.4$ eV, a relatively large conduction-band spike is present, which introduces a modest transport barrier for photogenerated electrons and slightly limits Voc and FF relative to the optimum. As χ increases toward 3.6 eV, the spike narrows to a magnitude that suppresses interface recombination without significantly impeding electron extraction, yielding the highest PCE obtained across all parameters examined in this study (19.92%, Figure 7, top panel). Beyond $\chi \approx 3.7$–3.8 eV, the conduction-band offset is estimated to invert into a cliff-like configuration, which is known to strongly enhance interface recombination by removing the barrier that otherwise separates photogenerated electrons from the ETL/absorber interface states; this is consistent with the sharp, near-linear collapse in Voc, FF, and PCE observed from $\chi = 3.8$ to 4.3 eV. The exact χ at which the spike-to-cliff transition occurs depends on the electron affinity of the ETL, which should be reported alongside this result.

Accordingly, while the raw numerical optimum of this sweep occurs at $\chi = 3.6$ eV, an absorber electron affinity of $\chi = 3.7$ eV — slightly beyond this numerical maximum — was adopted as the fixed baseline for subsequent simulations, providing a conservative margin against the spike-to-cliff transition described above, analogous to the safety-margin rationale used for the interface defect density baselines in Section 3.1.4. This result indicates that, among all device parameters examined thus far (Sections 3.1–3.5), band alignment at the ETL/absorber interface exerts the strongest single influence on power conversion efficiency, underscoring the importance of ETL selection and interface engineering in this device architecture.

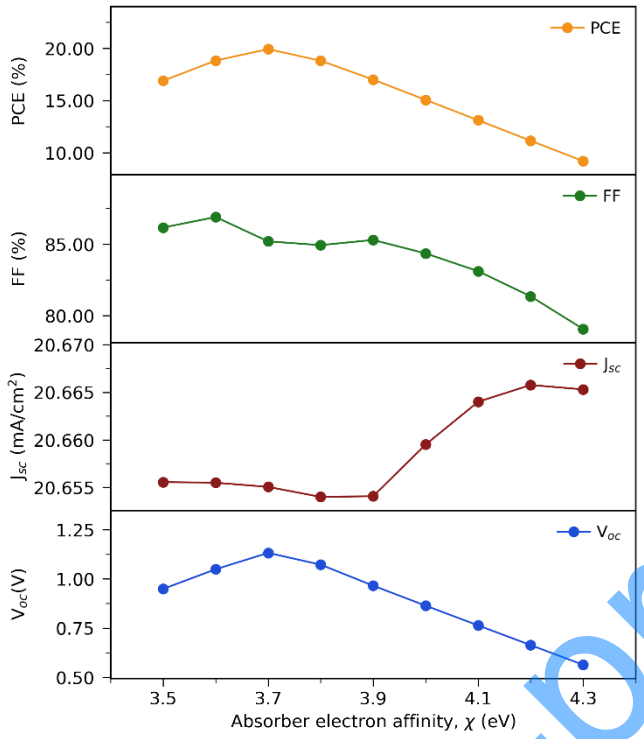

Fig. 7. Simulated photovoltaic parameters versus absorber electron affinity.

3.6. Impact of Absorber Electron Mobility on Photovoltaic Performance

With the absorber thickness, defect densities, doping density, and electron affinity fixed at their previously determined optimal values (Sections 3.1–3.5, $\chi = 3.7$ eV), the electron mobility (μn) of the YbZrSe3 absorber was first varied from 2 to 50 cm^2/Vs in 13 steps of 4 cm^2/Vs, and, since no saturation was observed over this range, a second sweep extended μn from 50 to 100 cm^2/Vs in 6 steps of 10 cm^2/Vs. The hole mobility was held fixed at 10 cm^2/Vs throughout, and the combined results (2–100 cm^2/Vs) are shown in Figure 8.

As shown in Figure 8, all four parameters continue to increase monotonically and smoothly with μn across the full extended range. Jsc increases from 17.161 mA/cm^2 at 2 cm^2/Vs to 18.519 mA/cm^2 at 100 cm^2/Vs (Figure 8, third panel), FF from 82.84% to 84.60% (Figure 8, second panel), and Voc marginally, from 1.1150 to 1.1168 V (Figure 8, bottom panel). Correspondingly, PCE rises from 15.85% to 17.50% (Figure 8, top panel), an absolute gain of 1.65 percentage points over the full range. This behavior is consistent with higher electron mobility reducing transport-limited

recombination losses and improving photogenerated-carrier collection efficiency at both short-circuit and maximum-power conditions, which raises Jsc and FF simultaneously; the comparatively small effect on Voc reflects that Voc in this device is governed primarily by interfacial and bulk recombination (Sections 3.1 and 3.3) rather than by carrier transport.

Although no plateau is reached within the tested range, the rate of improvement slows measurably between the two segments of the sweep: PCE increases at an average rate of ≈0.0208 percentage points per cm^2/Vs between 2 and 50 cm^2/Vs, versus ≈0.0130 percentage points per cm^2/Vs between 50 and 100 cm^2/Vs - a reduction of about 38% in slope. This indicates that the device is beginning to approach a transport-independent performance ceiling set by the other fixed parameters (Sections 3.1–3.5), even though full saturation is not yet reached at μn = 100 cm^2/Vs. Given the diminishing returns observed and the need to remain within physically plausible mobility values for this class of chalcogenide perovskites (for which only DFT-derived, not experimental, transport data currently exist), the sweep was not extended further, and μn = 100 cm^2/Vs was adopted as the fixed baseline value for subsequent simulations.

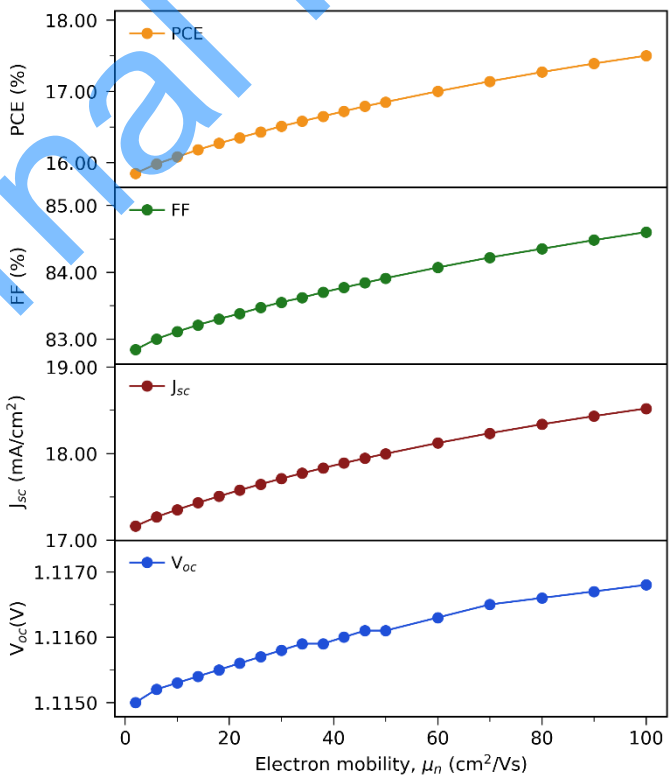

Fig. 8. Simulated photovoltaic parameters versus absorber electron mobility.

3.7. Energy Band Diagram at the Optimal Device Configuration

With all device parameters set to their optimal baseline values determined in Sections 3.1–3.6 (absorber thickness 0.7 μm; Nit = 10^{10} cm^{-2} at the ETL/absorber interface; Nit = 10^{11} cm^{-2} at the absorber/HTL interface; bulk defect density Nt = 10^{14} cm^{-3}; acceptor doping NA = 10^{17} cm^{-3}; electron affinity χ = 3.7 eV; electron mobility μn = 100 cm^2/Vs; hole mobility μp = 10 cm^2/Vs), the equilibrium energy band diagram of the complete device was generated (Figure 9).

As shown in Figure 9, a small conduction-band spike is present at the ETL/absorber interface (~0.2 μm), consistent with the near-optimal band alignment identified in Section 3.5 (χ = 3.7 eV): the spike is narrow enough to avoid significantly impeding electron extraction while still suppressing interfacial recombination. Across the quasi-neutral absorber region (~0.2–0.8 μm, consistent with the 0.7 μm optimized thickness of Section 3.2), the conduction and valence bands are essentially flat, and the electron and hole quasi-Fermi levels (EFn and EFp) remain closely and uniformly split, indicating low bulk recombination consistent with the Nt = 10^{14} cm^{-3} baseline established in Section 3.3. A pronounced downward band bending occurs near the absorber/HTL back interface (~0.8–0.9 μm), where the quasi-Fermi levels converge sharply - this is consistent with the absorber/HTL interface remaining the dominant recombination pathway identified in Section 3.1, even after full optimization of the remaining device parameters.

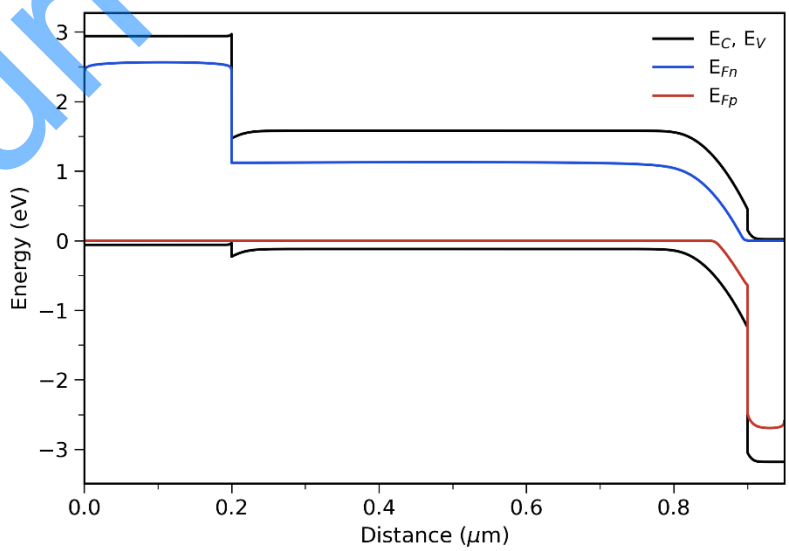

Fig. 9. Simulated equilibrium energy band diagram of the optimized device.

3.8. Recombination Currents at the Optimal Device Configuration

The voltage-dependent recombination current components of the fully optimized device are shown in Figure 10. The total recombination current (black) is dominated by recombination at the interfaces (magenta) across the entire simulated voltage range, with the two curves overlapping almost exactly: at V = 0, interfacial recombination accounts for 2.167 mA/cm^2 of the 2.223 mA/cm^2 total (97.5%), and at V = 1.112 V (close to Voc = 1.1168 V), it accounts for 17.672 mA/cm^2 of 17.740 mA/cm^2 (99.6%). Bulk Shockley–Read–Hall recombination (olive) remains three to four orders of magnitude below the interfacial component throughout the entire voltage range - only 0.0031 mA/cm^2 at V = 0 and 0.0075 mA/cm^2 near Voc - and, contrary to a first visual impression from the raw simulation output, never approaches the interfacial curve at any bias point; the vertical gap between the two curves is largest, not smallest, near Voc. The contact-limited minority-carrier currents Jn (red, left/ETL contact, ~3.6×10^{-4} mA/cm^2, essentially voltage-independent) and Jp (blue, right/HTL contact, 0.052–0.065 mA/cm^2) remain several orders of magnitude below the total recombination current throughout, confirming that ohmic-contact recombination is negligible in this device.

This result reinforces, and in fact strengthens, the central finding of Section 3.1.4: despite optimizing absorber thickness, bulk defect density, doping, electron affinity, and electron mobility (Sections 3.2–3.6), interfacial recombination accounts for essentially all (≥97.5%) of the total recombination current at every operating point from short-circuit to Voc, with its relative dominance over bulk SRH recombination actually increasing toward Voc. Further efficiency gains beyond the 17.50% achieved here would almost certainly require direct interfacial passivation or a lower-defect-density absorber/HTL contact, rather than further bulk or transport-property optimization, since the latter is shown here to have only a marginal effect on the dominant loss channel.

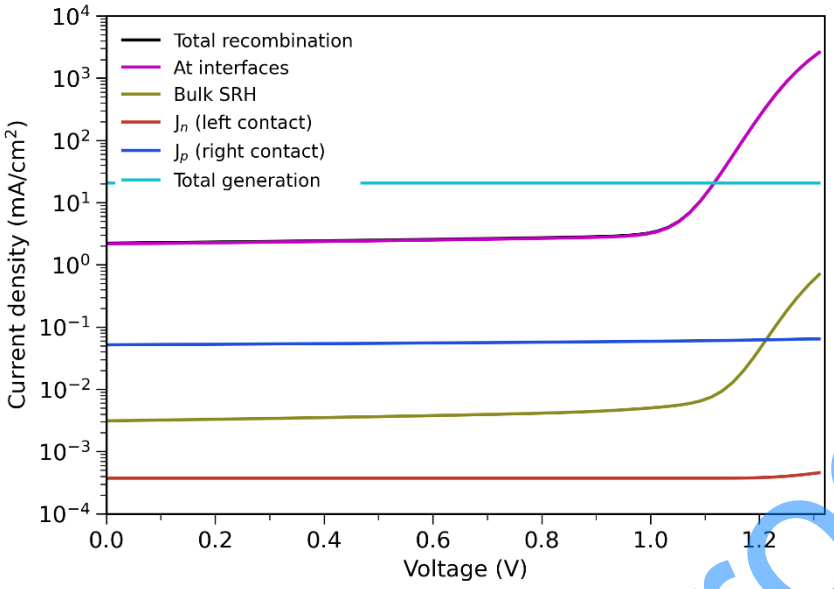

Fig. 10. Simulated voltage-dependent recombination current components of the optimized device.

3.9. Quantum Efficiency of the Optimal Device Configuration

The simulated external quantum efficiency (QE) spectrum of the optimized device under short-circuit conditions is shown in Figure 11.

As shown in Figure 11, the device exhibits a broad, high quantum-efficiency response across the visible spectrum, rising from 88.05% at 300 nm to a peak of 95.68% at 390 nm, and remaining above 90% from approximately 380 to 550 nm (89.33% at 550 nm). The comparatively high blue-response (>93% below 450 nm) indicates low front-surface recombination loss, consistent with the small, near-optimal conduction-band spike at the ETL/absorber interface identified in Sections 3.5 and 3.7. QE declines gradually from 89.33% at 550 nm to 78.18% at 650 nm and 61.55% at 700 nm, then falls sharply to 42.58% at 720 nm and effectively zero by 730 nm. This cutoff is in excellent agreement with the absorber bandgap (Eg = 1.7 eV): the corresponding absorption-edge wavelength, $\lambda g = hc/Eg$, is 729.3 nm, matching the simulated QE cutoff (between the 720 nm and 730 nm data points) to within the 10 nm resolution of the simulation and confirming internal consistency of the optical and electronic model parameters used throughout this study.

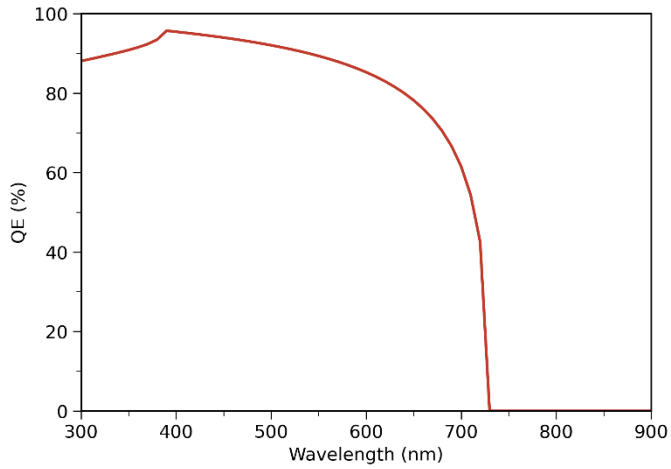

Fig. 11. Simulated external quantum efficiency spectrum of the optimized device.

3.10. Summary of Optimized Device Parameters and Final Performance

Table 4 summarizes the baseline device parameters obtained sequentially in Sections 3.1–3.6, each optimized while holding the previously determined parameters fixed. The final, fully optimized device configuration achieves Voc = 1.1168 V, Jsc = 18.5187 mA/cm^2, FF = 84.60%, and PCE = 17.50%, representing the overall performance ceiling identified for this device architecture within the scope of the present study.

Table 4. Optimized device parameters and final photovoltaic performance.

Parameter	**Optimized value**
Absorber thickness	0.7 μm
N_{it} - ETL/absorber interface	10^{10} cm^{-2}
N_{it} - absorber/HTL interface	10^{11} cm^{-2}
N_t - absorber bulk defect density	10^{14} cm^{-3}
N_A - absorber acceptor doping	10^{17} cm^{-3}
χ - absorber electron affinity	3.7 eV
μ_n - absorber electron mobility	100 cm^2/Vs
μ_p - absorber hole mobility	10 cm^2/Vs
V_{oc} (final)	1.1168 V
J_{sc} (final)	18.5187 mA/cm^2
FF (final)	84.60%
PCE (final)	17.50%

Overall, this systematic, sequential optimization study substantially improved device performance relative to the unoptimized, high-defect-density condition established in Section 3.1 (PCE = 14.05%), reaching a final value of 17.50% once absorber thickness, bulk defect density, doping, band alignment, and carrier transport were each optimized in turn. Among the individual sweeps, band-alignment optimization (Section 3.5) produced the largest single-parameter improvement observed in this study, and the recombination analysis in Sections 3.8 confirms - consistent with Section 3.1 - that residual interfacial recombination at the absorber/HTL junction remains the primary factor limiting further efficiency gains in this device architecture.

4. Conclusions

This study presented a systematic, SCAPS-1D-based sequential optimization of a $YbZrSe_3$ thin-film solar cell, providing the first comprehensive device-level performance benchmark for this emerging lead-free chalcogenide absorber. Optimizing interface defect density, absorber thickness, bulk defect density, acceptor doping density, electron affinity, and electron mobility in turn raised the simulated power conversion efficiency from 14.05% at baseline high-defect conditions to a final value of 17.50%, with an open-circuit voltage of 1.1168 V, a short-circuit current density of 18.52 mA/cm^2, and a fill factor of 84.60%.

Across all sweeps, the absorber/HTL interface consistently emerged as the dominant loss channel: it degraded roughly three times faster than the ETL/absorber interface, tolerated nearly two orders of magnitude lower defect density before appreciable loss, and accounted for more than 97% of total recombination current even after full optimization. The absorber bulk defect density instead showed a sharp, threshold-like collapse, remaining largely inert below 10^{14} cm^{-3} before precipitating rapid loss at higher densities. Band alignment at the ETL/absorber interface produced the single largest efficiency gain, with a narrow conduction-band spike near an electron affinity of 3.7 eV balancing recombination suppression against electron extraction, while the doping sweep alone produced a

genuine interior optimum at 10^{17} cm^{-3}, reflecting the trade-off between voltage gain and current loss. Quantum efficiency simulations confirmed broad, efficient photon-to-carrier conversion consistent with the absorber's 1.7 eV bandgap.

Overall, these results establish absorber/HTL interface passivation as the most critical target for further improving $YbZrSe_3$-based photovoltaics, and the sequential optimization framework developed here offers a validated methodology and quantitative baseline to guide subsequent studies of this and related chalcogenide absorber materials. More broadly, this work illustrates the value of pairing recently proposed, first-principles-identified absorber materials with defect-aware device-level simulation: by providing quantitative defect-density thresholds, band-alignment targets, and a realistic performance benchmark well ahead of experimental realization, studies of this kind can directly inform and accelerate future synthesis and device-fabrication efforts for $YbZrSe_3$ and related emerging chalcogenide perovskites.

References

[1] Green, M. A., et al. (2025). Solar cell efficiency tables (Version 66). *Progress in Photovoltaics: Research and Applications*, 33, 795–810. https://doi.org/10.1002/pip.3919

[2] Agarwal, S., Vincent, K. C., & Agrawal, R. (2025). From synthesis to application: A review of $BaZrS_3$ chalcogenide perovskites. *Nanoscale*, 17, 4250–4300. https://doi.org/10.1039/D4NR03880K

[3] Sun, Y.-Y., Agiorgousis, M. L., Zhang, P., & Zhang, S. (2015). Chalcogenide perovskites for photovoltaics. *Nano Letters*, 15, 581–585. https://doi.org/10.1021/nl504046x

[4] Nishigaki, Y., Nagai, T., Nishiwaki, M., Aizawa, T., Kozawa, M., Hanzawa, K., Kato, Y., Sai, H., Hiramatsu, H., & Hosono, H. (2020). Extraordinary strong band-edge absorption in distorted chalcogenide perovskites. *Solar RRL*, 4, 1900555. https://doi.org/10.1002/solr.201900555

[5] Comparotto, C., Davydova, A., Ericson, T., Riekehr, L., Moro, M. V., Kubart, T., & Scragg, J. J. (2020). The chalcogenide perovskite $BaZrS_3$: Thin film growth by sputtering and rapid thermal

processing. *ACS Applied Energy Materials*, 3, 2762–2770. https://doi.org/10.1021/acsaem.9b02428

[6] Wei, X., Hui, H., Perera, S., Sheng, A., Watson, D. F., Sun, Y.-Y., Jia, Q., Zhang, S., & Zeng, H. (2020). Ti-alloying of $BaZrS_3$ chalcogenide perovskite for photovoltaics. *ACS Omega*, 5, 18579–18583. https://doi.org/10.1021/acsomega.0c00740

[7] Li, Q., Wu, H., Li, W., Zhang, J., & Sa, R. (2025). Computational discovery of novel chalcogenide perovskites $YbMX_3$ (M = Zr, Hf; X = S, Se) for optoelectronics. *Molecules*, 30, 1468. https://doi.org/10.3390/molecules30071468

[8] Burgelman, M., Nollet, P., & Degrave, S. (2000). Modelling polycrystalline semiconductor solar cells. *Thin Solid Films*, 361–362, 527–532. https://doi.org/10.1016/S0040-6090(99)00825-1

[9] Burgelman, M., Decock, K., Khelifi, S., & Abass, A. (2013). Advanced electrical simulation of thin film solar cells. *Thin Solid Films*, 535, 296–301. https://doi.org/10.1016/j.tsf.2012.10.032

[10] Sherkar, T. S., Momblona, C., Gil-Escrig, L., Ávila, J., Sessolo, M., Bolink, H. J., & Koster, L. J. A. (2017). Recombination in perovskite solar cells: Significance of grain boundaries, interface traps, and defect ions. *ACS Energy Letters*, 2, 1214–1222. https://doi.org/10.1021/acsenergylett.7b00236

[11] Karthick, S., Velumani, S., & Bouclé, J. (2022). Chalcogenide $BaZrS_3$ perovskite solar cells: A numerical simulation and analysis using SCAPS-1D. *Optical Materials*, 126, 112250. https://doi.org/10.1016/j.optmat.2022.112250

[12] Chandrakar, A., & Khare, A. (2026). Highly efficient dual-absorber $BaZrS_3$/$CaZrSe_3$ chalcogenide perovskite solar cells: A SCAPS-1D simulation study. *Journal of Materials Science: Materials in Electronics*, 37, 980. https://doi.org/10.1007/s10854-026-17385-8

[13] Mercy, E. N. V., Srinivasan, D., & Marasamy, L. (2024). Emerging $BaZrS_3$ and $Ba(Zr,Ti)S_3$ chalcogenide perovskite solar cells: A numerical approach toward device engineering and unlocking efficiency. *ACS Omega*, 9, 4359–4376. https://doi.org/10.1021/acsomega.3c06627

[14] Aly, K. A., Thakur, N., Kumar, P., Saddeek, Y., Shater, T., Ismail, Y. A. M., & Sharma, P.

(2024). Optimizing solar cell performance with chalcogenide perovskites: A numerical study of $BaZrSe_3$ absorber layers. *Solar Energy*, 282, 112961. https://doi.org/10.1016/j.solener.2024.112961

[15] Srinivasan, D., Rasu Chettiar, A.-D., Vincent Mercy, E. N., & Marasamy, L. (2025). Scrutinizing the untapped potential of emerging $ABSe_3$ (A = Ca, Ba; B = Zr, Hf) chalcogenide perovskites solar cells. *Scientific Reports*, 15, 3454. https://doi.org/10.1038/s41598-024-80473-4

[16] Ali, A., Iqbal, M. J., Zakaly, H. M. H., Almutairi, B. S., & Ali, S. (2026). Interface and band engineering of $CuTlS_2$ chalcopyrite solar cells using SnS_2/NiO transport layers. *Materials Today Communications*, 54, 115689. https://doi.org/10.1016/j.mtcomm.2026.115689

[17] Chawki, N., Essajai, R., Rouchdi, M., Braiche, M., Al-Hattab, M., & Fares, B. (2024). Efficacy analysis of $BaZrS_3$-based perovskite solar cells: Investigated through a numerical simulation. *Advances in Materials and Processing Technologies*, 11, 389–402. https://doi.org/10.1080/2374068X.2024.2307093

[18] Niemegeers, A., & Burgelman, M. (1996). Numerical modelling of AC-characteristics of CdTe and CIS solar cells [Paper presentation]. 25th IEEE Photovoltaic Specialists Conference, Washington, DC, USA. https://doi.org/10.1109/PVSC.1996.564274

[19] Degrave, S., Burgelman, M., & Nollet, P. (2003). Modelling of polycrystalline thin film solar cells: New features in SCAPS version 2.3 [Paper presentation]. 3rd World Conference on Photovoltaic Energy Conversion, Osaka, Japan. ISBN 4-9901816-0-3

[20] Decock, K., Khelifi, S., & Burgelman, M. (2011). Modelling multivalent defects in thin film solar cells. *Thin Solid Films*, 519, 7481–7484. https://doi.org/10.1016/j.tsf.2010.12.039

[21] Verschraegen, J., & Burgelman, M. (2007). Numerical modeling of intra-band tunneling for heterojunction solar cells in SCAPS. *Thin Solid Films*, 515, 6276–6279. https://doi.org/10.1016/j.tsf.2006.12.049

[22] Gummel, H. K. (1964). A self-consistent iterative scheme for one-dimensional steady state transistor calculations. *IEEE Transactions on Electron Devices*, ED-11, 455–465.

https://doi.org/10.1109/T-ED.1964.15364

[23] Shockley, W., & Read, W. T. (1952). Statistics of the recombinations of holes and electrons. *Physical Review*, 87, 835–842. https://doi.org/10.1103/PhysRev.87.835

[24] Hall, R. N. (1952). Electron-hole recombination in germanium. *Physical Review*, 87, 387. https://doi.org/10.1103/PhysRev.87.387

[25] Zhu, Y., Deng, K., Sun, H., Gu, B., Lu, H., Cao, F., Xiong, J., & Li, L. (2018). TiO2 phase junction electron transport layer boosts efficiency of planar perovskite solar cells. *Advanced Science*, 5, 1700614. https://doi.org/10.1002/advs.201700614

[26] Nakka, L., Cheng, Y., Aberle, A. G., & Lin, F. (2022). Analytical review of Spiro-OMeTAD hole transport materials: Paths toward stable and efficient perovskite solar cells. *Advanced Energy and Sustainability Research*, 3, 2200045. https://doi.org/10.1002/aesr.202200045

[27] Chavan, G. T., Kim, Y., Khokhar, M. Q., Hussain, S. Q., Cho, E.-C., Yi, J., Ahmad, Z., Rosaiah, P., & Jeon, C.-W. (2023). A brief review of transparent conducting oxides (TCO): The influence of different deposition techniques on the efficiency of solar cells. *Nanomaterials*, 13, 1226. https://doi.org/10.3390/nano13071226

[28] Anderson, R. L. (1962). Experiments on Ge-GaAs heterojunctions. *Solid-State Electronics*, 5, 341–351. https://doi.org/10.1016/0038-1101(62)90115-6

[29] ASTM International. (2020). Standard tables for reference solar spectral irradiances: Direct normal and hemispherical on 37° tilted surface (ASTM G173-03(2020)). ASTM International. https://doi.org/10.1520/G0173-03R20

[30] Sze, S. M., & Ng, K. K. (2007). *Physics of semiconductor devices* (3rd ed.). John Wiley & Sons. ISBN 978-0-471-14323-9.

[31] Burgelman, M., & Marlein, J. (2008). Analysis of graded band gap solar cells with SCAPS [Paper presentation]. 23rd European Photovoltaic Solar Energy Conference, Valencia, Spain. https://doi.org/10.4229/23RDEUPVSEC2008-3DO.5.2